

Three-dimensional numerical simulation for an open channel flow with a constriction

Simulation numérique tridimensionnelle pour un écoulement dans un canal à surface libre avec rétrécissement

N. J. SHANKAR, *Professor, Department of Civil Engineering, National University of Singapore, Singapore 119260.*

E. S. CHAN, *Associate professor, Department of Civil Engineering, National University of Singapore, Singapore 119260.*

Q. Y. ZHANG, *Research scholar, Department of Civil Engineering, National University of Singapore, Singapore 119260.*

ABSTRACT

Flow characteristics in an open channel with a constriction are investigated numerically by using a three-dimensional multi-level hydrodynamic model. In this model, the two-step Euler predictor-corrector algorithm is introduced to predict and correct free surface water level. The momentum equations in horizontal directions are discretized in an explicit scheme for the component velocities u and v , and the continuity equation is discretized for the velocity w in an implicit scheme in uniform and non-uniform grid systems. The model has been tested against analytical solutions for two standard cases and used to study sudden contraction and expansion open channel flow. The numerical results are in good agreement with analytical and experimental data. Simulated flow patterns for the sudden contraction and expansion flow show reasonable flow characteristics downstream of an opening.

RÉSUMÉ

Les caractéristiques de l'écoulement dans un canal à surface libre avec un rétrécissement sont étudiées numériquement en utilisant un modèle hydrodynamique tridimensionnel multi-niveaux. Dans ce modèle, on introduit l'algorithme prédicteur-correcteur d'Euler à deux pas, pour prédire et corriger le niveau de la surface libre. Les équations dynamiques horizontales sont discrétisées avec un schéma explicite pour les composantes de vitesse u et v , et l'équation de continuité est discrétisée, pour la composante w , avec un schéma implicite, dans des systèmes de grilles uniformes et non uniformes. Le modèle a été testé sur des solutions analytiques pour deux cas standards et utilisé pour étudier le rétrécissement et l'élargissement brusque d'un écoulement à surface libre en canal. Les résultats numériques sont en bon accord avec les données analytiques et expérimentales. Les configurations d'écoulement simulées pour le rétrécissement et l'élargissement brusque présentent des caractéristiques raisonnables pour un écoulement à l'aval d'une ouverture.

1 Introduction

Flow patterns in rivers and navigation channels are greatly influenced when large-scale structures such as piers, causeways or groins are constructed across them. Flow velocity changes rapidly near the structures because the cross-sections of the flow channel are suddenly adjusted. A typical scenario is the sudden contraction and expansion of flow such as that shown in Fig. 1. When water flows through an opening, upstream water will head up from the side walls and bottom resulting in a rapid increase in the flow velocity. Beyond the opening, however, flow separation from solid boundaries will ensue and large-scale eddies will be formed in the horizontal and vertical directions. These eddies cause strong scouring and erosion of the bed and the foundations of hydraulic structures, thus undermining the safety of the structures. In the design of such structures, a good understanding of the hydraulic characteristics would be necessary.

Since it is expensive and time consuming to conduct physical model tests and field measurements, many mathematical hydrodynamic models have been developed and applied to solve open channel flow problems in the past three decades. Most of these models are two-dimensional depth or width averaged models. Flow patterns around a long jetty or a groin have been studied by using the two-dimensional depth averaged models (Shinji, 1996; Zhou and John, 1992). The research results show that the horizontal eddy occurs behind the long jetty or groin. Flow Patterns of buoyant jet flows have also been obtained by applying the two-

dimensional width averaged models (Adams and Rodi, 1990; Karpik and Raithby, 1990). The simulation results show that an eddy in the vertical direction exists. As may be anticipated, the two-dimensional models cannot provide a good simulation of the complex problem depicted by Fig. 1. A three-dimensional mathematical model would be necessary.

There exist, however, some difficulties in applying three-dimensional models. Efficient computational schemes and finer grid resolution are required because of the large body of moving water and the rapid changes of the cross section. Length scales normally measured in kilometers must be divided into many small grids

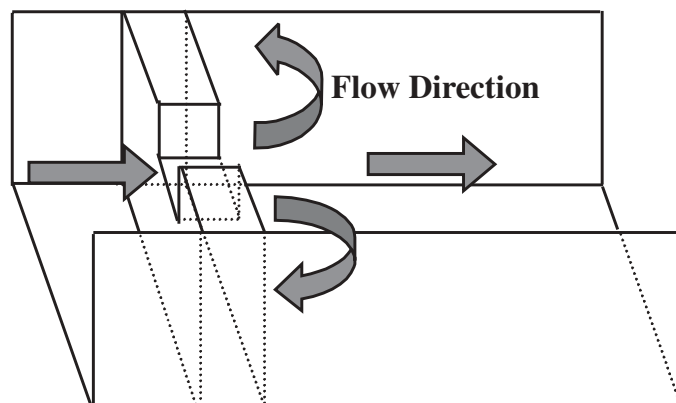


Fig. 1. Sudden Contraction and Expansion.

Revision received April 12, 1999. Open for discussion till August 31, 2001.

and numerically dealt with. Many three-dimensional models for free surface flow problems have been developed in the past (Cao and Zhang, 1987; Kawahara et al., 1983; Kim and Lee, 1994; Tomaya and Pun, 1992). Amongst the pioneer models developed was the model by Leendertse et al. (1973) which was based on rigid-lid approximations. The latter is, however, inappropriate for problems with large temporal fluctuations in the free surface. Coordinate transformations in both the horizontal and vertical scales have since been introduced to resolve this limitation and to better fit the irregular boundary of the model domain. But these transformations increase computational time and also induce numerical uncertainties (Cheng and Smith, 1989). In order to offset these disadvantages, a multi-layer or a multi-level model is widely used in three-dimensional hydrodynamic simulations. The free surface boundary does not need to be specially dealt with because the three-dimensional structure in both the multi-level and the multi-layer models involves stacking of many depth averaged hydrodynamic models. The multi-layer model is different from the multi-level model in the construction of the interfacial layer. In the multi-layer model, there is no transport across the layers that displace vertically to maintain continuity. The application of a multi-layer model to simulate tidal currents requires the strict specification of open boundary conditions at the layer interfaces, which is rather difficult in practical situations. However the above difficulties are not encountered in the case of a multi-level model. The multi-level model assumes that the interfacial layers are fixed in space and there is vertical transport between layers to maintain continuity.

To date, many numerical techniques which involve finite difference, finite element and finite analysis methods are used to solve the basic governing equations in a large number of three-dimensional hydrodynamic models. The main advantage of using finite element and finite analysis methods is the ease in simulating complex bathymetries (Daniel and Francisco, 1987; Fang, 1994; Mutsuto and Kenichi, 1978). However, the program codes are complicated, and these models also require much larger computer memory and considerable computer time. The finite difference method has been used extensively in the last two decades. The main advantage of using a finite difference scheme is its simplicity and ease in programming. Various techniques have been developed to improve the stability and resolution of finite difference schemes (Cao and Zhang, 1987; Kim and Lee, 1994; Shankar et al., 1995; Zhang, 1998). Time marching schemes, used in three-dimensional hydrodynamic models, can be classified into three classes, i.e., the implicit scheme, semi-implicit scheme and explicit scheme. The computational procedure in the implicit scheme or semi-implicit scheme is more stable, but these schemes are time consuming since there is a need to solve the simultaneous algebraic equation system. Moreover, the computational core storage requirement in the implicit scheme and semi-implicit scheme is much more than that in the explicit scheme. Considering these, the explicit scheme or semi-implicit numerical scheme is preferable for most practical computations.

In this study, an efficient and simple three-dimensional finite difference multi-level model is developed. A two-step Euler predictor-corrector algorithm with second-order accuracy in time step-

length is introduced to predict and correct free surface water level accurately and rapidly. The momentum equations in the horizontal directions are discretized with an explicit scheme, and the continuity equation is discretized with an implicit scheme. The velocity components in the x , y and z directions are directly obtained without solving an algebraic equation system. The distinguishing features of the proposed numerical method are the higher accuracy and stability compared to a complete explicit scheme and the reduced computational time compared with semi-implicit and fully implicit schemes. The model is tested against analytical solutions for two standard cases in a rectangular basin. These are wind induced circulation and tide induced flow. The model is also used to simulate the flow in a channel with a sudden contraction and expansion.

2 Governing differential equations

Under the conditions of hydrostatic pressure distribution, the Reynolds time-averaged Navier-Stokes equations and the introduction of the eddy viscosity concept for Reynolds stress, the governing equations of continuity and momentum for incompressible turbulent fluid flow in a three-dimensional (x , y , z) coordinate system with the z axis directed vertically upwards are:

$$\frac{\partial u}{\partial x} + \frac{\partial v}{\partial y} + \frac{\partial w}{\partial z} = 0 \quad (1)$$

$$\begin{aligned} \frac{\partial u}{\partial t} + u \frac{\partial u}{\partial x} + v \frac{\partial u}{\partial y} + w \frac{\partial u}{\partial z} + \frac{1}{\rho} \frac{\partial p}{\partial x} - fv - \\ \frac{\partial}{\partial x} (\epsilon_x \frac{\partial u}{\partial x}) - \frac{\partial}{\partial y} (\epsilon_y \frac{\partial u}{\partial y}) - \frac{\partial}{\partial z} (\epsilon_z \frac{\partial u}{\partial z}) = 0 \end{aligned} \quad (2)$$

$$\begin{aligned} \frac{\partial v}{\partial t} + u \frac{\partial v}{\partial x} + v \frac{\partial v}{\partial y} + w \frac{\partial v}{\partial z} + \frac{1}{\rho} \frac{\partial p}{\partial y} + fu - \\ \frac{\partial}{\partial x} (\epsilon_x \frac{\partial v}{\partial x}) - \frac{\partial}{\partial y} (\epsilon_y \frac{\partial v}{\partial y}) - \frac{\partial}{\partial z} (\epsilon_z \frac{\partial v}{\partial z}) = 0 \end{aligned} \quad (3)$$

$$g = -\frac{1}{\rho} \frac{\partial p}{\partial z} \quad (4)$$

in which p = the time-averaged water pressure; u , v , w = time-averaged velocity components in x , y and z directions; f = coriolis force coefficient; in practical application, ϵ_x and ϵ_y are usually assumed to be equal to ϵ_h ; ϵ_h , ϵ_z = horizontal and vertical eddy viscosity coefficients; ρ = water density; g = acceleration due to gravity; t = time.

After substituting Eq. (4) into Eqs. (2) and (3), and taking the vertical integration of Eqs. (1) to (3) over a discrete layer of thickness h_k (as shown in Fig. 2), and also using a streamline condition at the free surface and the bottom, the governing equations become:

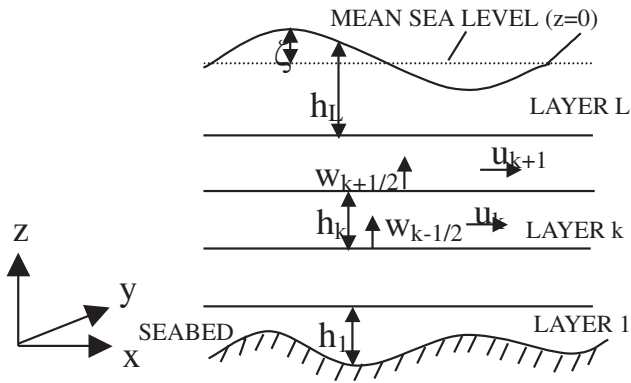


Fig. 2. Definition of Vertical Coordinate System

$$w_{k+\frac{1}{2}} = w_{k-\frac{1}{2}} - \left[\frac{\partial(uh_k)}{\partial x} \right]_k - \left[\frac{\partial(vh_k)}{\partial y} \right]_k \quad (5)$$

$$\begin{aligned} \frac{\partial u}{\partial t} + \frac{1}{h_k} \left(\frac{\partial(uuh_k)}{\partial x} + \frac{\partial(uvh_k)}{\partial y} \right) + (wu)_{k+\frac{1}{2}} - (wu)_{k-\frac{1}{2}} - fv \\ + g \frac{\partial \zeta}{\partial x} - \varepsilon_h \left(\frac{\partial^2 u}{\partial x^2} + \frac{\partial^2 u}{\partial y^2} \right) - \frac{1}{h_k} \left[\left(\frac{\tau_x}{\rho} \right)_{k+\frac{1}{2}} - \left(\frac{\tau_x}{\rho} \right)_{k-\frac{1}{2}} \right] = 0 \end{aligned} \quad (6)$$

$$\begin{aligned} \frac{\partial v}{\partial t} + \frac{1}{h_k} \left(\frac{\partial(uvh_k)}{\partial x} + \frac{\partial(vvh_k)}{\partial y} \right) + (wv)_{k+\frac{1}{2}} - (wv)_{k-\frac{1}{2}} + fu \\ + g \frac{\partial \zeta}{\partial y} - \varepsilon_h \left(\frac{\partial^2 v}{\partial x^2} + \frac{\partial^2 v}{\partial y^2} \right) - \frac{1}{h_k} \left[\left(\frac{\tau_y}{\rho} \right)_{k+\frac{1}{2}} - \left(\frac{\tau_y}{\rho} \right)_{k-\frac{1}{2}} \right] = 0 \end{aligned} \quad (7)$$

The streamline conditions at the surface and the bottom:

$$\left. \frac{\partial \zeta}{\partial t} \right|_{z=\zeta} = w_\zeta - u \frac{\partial \zeta}{\partial x} - v \frac{\partial \zeta}{\partial y}; \quad \left. (w + u \frac{\partial H}{\partial x} + v \frac{\partial H}{\partial y}) \right|_{z=-H} = 0$$

where H = the water depth below the reference plane (Mean Sea Level), ζ = water level at the free surface.

If the individual layer continuity equations are summed over the entire water column, the internal vertical velocities cancel out and this leads to:

$$\frac{\partial U}{\partial x} + \frac{\partial V}{\partial y} + \frac{\partial \zeta}{\partial t} = 0 \quad (8)$$

where

$$U = \int_{-H}^{\zeta} u dz, \quad V = \int_{-H}^{\zeta} v dz;$$

for bottom layer, $h_k = h(x, y)$; for top layer, $h_k = h(x, y, t)$; for interior layers, $h_k = \text{constant}$;

$$\tau_x = \rho \varepsilon_z \frac{\partial u}{\partial z}; \quad \tau_y = \rho \varepsilon_z \frac{\partial v}{\partial z}.$$

The shear stress at the surface is given by:

$$\tau_{sx} = \rho_a c_s W_x \sqrt{W_x^2 + W_y^2} \quad \text{and} \quad \tau_{sy} = \rho_a c_s W_y \sqrt{W_x^2 + W_y^2}$$

where c_s = wind stress coefficient; W_x, W_y = the component wind speeds in x and y directions respectively, ρ_a = the mass density of air.

Assuming that shear stress is a quadratic function of the bed velocity, the imposed relation can be written in the following form:

$$\tau_{bx} = \rho c_b u_b \sqrt{u_b^2 + v_b^2} \quad \text{and} \quad \tau_{by} = \rho c_b v_b \sqrt{u_b^2 + v_b^2}$$

in which c_b = the bottom friction coefficient; u_b, v_b = the layer-averaged velocity components in x and y directions respectively near the bottom.

To solve the above governing equations, boundary conditions must be imposed. In general, two types of boundary conditions are to be distinguished: closed and open boundaries. Closed boundaries are land-water boundaries and open boundaries refer to water-water boundaries introduced to restrict the size of the problem domain. At the closed boundaries, the slip or no-slip boundary condition is adopted. At the open boundaries, the velocity or water level must be prescribed.

3 Numerical methodology

The layer-averaged equations derived in section 2 are solved on a three-dimensional space-staggered grid (Fig. 3). The horizontal grid spacing is uniform or non-uniform, and the vertical grid spacing can also be variable. The horizontal velocities u and v are defined at the center of each layer and the vertical velocity w is defined at the layer interfaces. Three time-levels are involved in the predictor finite difference equation, the previous time level, the present time level and the advanced time level. Two time-levels are used in other finite difference equations, the present time level and the advanced time level. The upwind difference scheme for the spatial convective terms of the momentum equations, central difference for the other spatial derivative terms and central and forward difference for the time derivative terms are adopted. For the boundary points, four-point high accuracy interpolation formulas are used in the convective terms. In order to save computational time and improve accuracy, the two-step Euler predictor-corrector algorithm is introduced to solve the finite difference equations. All finite difference equations are given in Appendix III. The computational process is depicted as follows:

1. set spatial and temporal grids $\Delta x, \Delta y, h_k, \Delta t$.
2. set initial conditions, boundary conditions and parameters.
3. predict the free surface by using the equation ((III-1) or (III-2)).
4. solve x direction momentum finite difference equation for u^{n+1} by using the equation (III-5).
5. solve y direction momentum finite difference equation for v^{n+1} by using the equation (III-6).

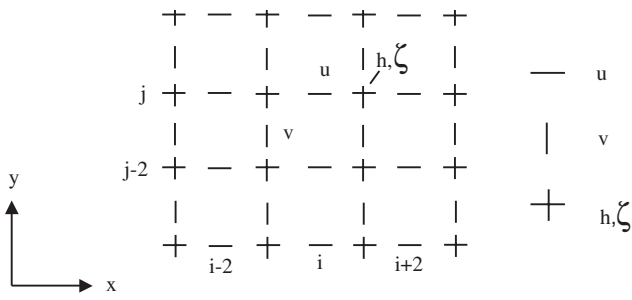


Fig. 3(a) x,y Plane

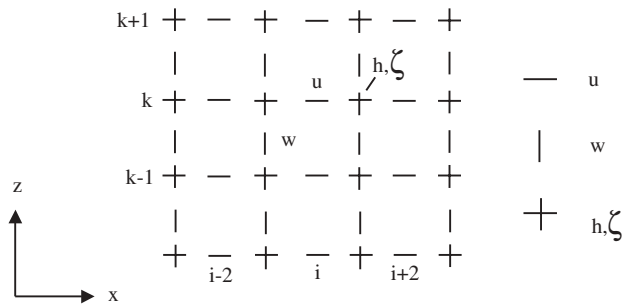


Fig. 3(b) x,z Plane

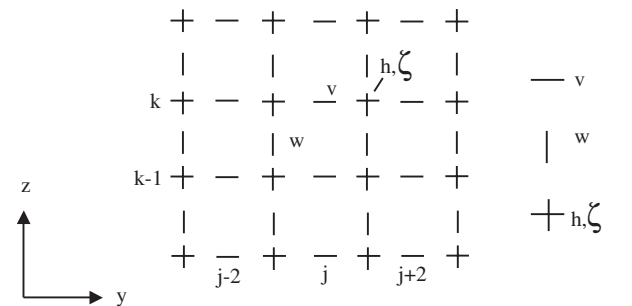


Fig. 3(c) y,z Plane

Fig. 3. Layout of the Grid

6. solve the continuity equation for w^{n+1} and correct ζ^{n+1} by the equations ((III-4) and (III-3)).
7. start new time loop

4 Model verifications

4.1 Numerical experiment 1: Wind-induced circulation

Before attempting to apply the 3-D multi-level hydrodynamic model to engineering problems it is desirable to prove its accuracy and efficiency by applying it to some standard cases for which the analytical solutions exist. At first, the model is applied to wind induced circulation in a rectangular closed basin (as shown in Fig. 4). Using the no-slip condition at the channel bed, the following uniform and steady state analytical solution for horizontal velocity component in a well-mixed channel with constant vertical eddy viscosity ϵ is known (Li and Zhan, 1993; Lu and Wai, 1995):

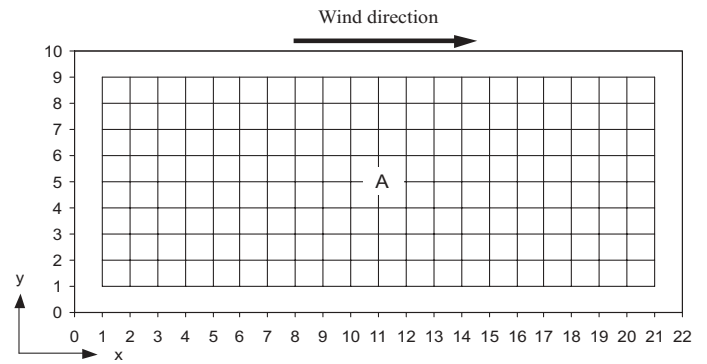


Fig. 4. Horizontal mesh used for the simulation of wind induced circulation

$$u = \tau_{xz}^s \sigma (h + \zeta) (3\sigma - 2) / 4\epsilon\rho \quad (9)$$

where u = horizontal velocity in x direction; h = water depth; ζ = the free water surface elevation above the water depth; $\sigma = (h+z)/(h+\zeta)$; ϵ = eddy viscosity coefficient in vertical direction; τ_{xz}^s surface wind stress.

A rectangular basin with a depth of 10 m, a length of 2 km, and a width of 0.8 km was simulated. The free surface was acted on by a constant wind-induced stress (1.5 N/m^2). The water body was divided into ten equal layers and the following parameters were adopted: $\Delta x = \Delta y = 100 \text{ m}$; $\Delta t = 5 \text{ s}$; $\epsilon_h = 0$; $\epsilon_z = 0.01 \text{ m}^2/\text{s}$; $f = 0$; $\rho = 1000 \text{ kg/m}^3$. The convergence was reached from a cold start after the program was run for eight time-step lengths. The simulated steady state vertical velocity profile at the center of the channel and the corresponding analytical solution was shown in Fig. 5. It can be seen that the computed results agree very well with the analytical solution. The flow velocities in the vertical direction change from the maximum value at the water surface to zero at about 6.7 m of the water depth, then the flow direction changes below 6.7 m.

4.2 Numerical experiment 2: Tide-induced circulation

This numerical experiment is concerned with the three-dimensional unsteady flow in a rectangular channel driven by tidal forc-

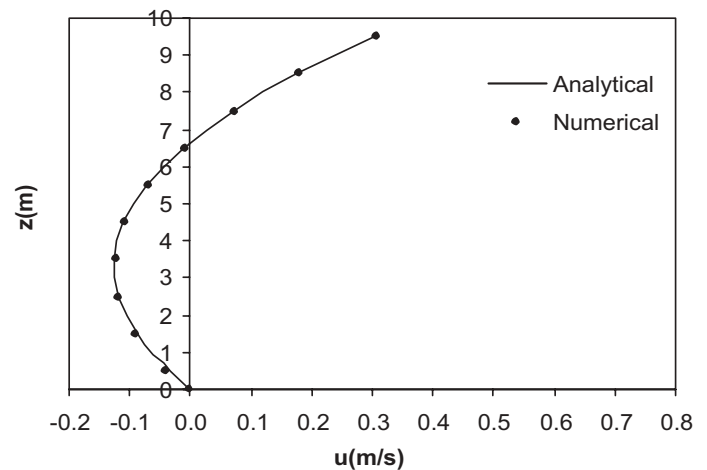


Fig. 5. Comparison of analytical and computed u -velocity profiles at A (Fig. 4)

ing at the open boundary. A rectangular basin with a depth of 10m, a length of 3400m, and a width of 1400m was simulated. The problem geometry and the horizontal mesh are shown in Fig. 6. A cosine wave with a maximum amplitude of 0.5m at the right open boundary was introduced as free water surface elevation at time $t = 0$. The analytical solution for this flow situation consists of the following equations (Ippen, 1966):

$$\zeta = A \cos(\omega t) \quad (10)$$

$$u(x,t) = \frac{A\omega x}{h} \sin(\omega t) \quad (11)$$

where A is the wave amplitude, ω is the angular frequency ($\frac{2\pi}{T}$), h is the water depth, x is the distance from the left boundary, t is time and T is the wave period, ζ is water surface elevation above still water level and u is the depth averaged velocity component in the x direction.

In the numerical simulations, the water body was divided into seven equal layers and the following parameters were adopted: $\Delta x = 200$ m; $\Delta y = 100$ m; $\Delta t = 5$ s; $\epsilon_z = 0.01$ m²/s; $\epsilon_h = 0$; $f = 0$; $\rho = 1000$ kg/m³; $T = 12$ hours. To give better simulation for unsteady water flow near the left solid boundary, a non-uniform grid was used and Δx was decreased to 100m. Convergent results were obtained after a half tidal period of simulation from a cold start. After the simulation of one tidal period, the velocity of every layer at the center of the channel was integrated and averaged in depth at the end of every hour. The numerical and analytical results of free water surface elevation and depth-averaged velocities were compared in Fig. 7. The analytical and numerical values are almost identical. The comparisons of the numerical results with the analytical results show that the maximum water surface elevations agree to within 2.5% and the maximum u -velocity components are correct to within 1%.

5 Application to an open channel flow with a constriction

5.1 Experimental investigation

The objectives of the experimental investigation are not to duplicate a specific prototype problem. The focus, instead, is on two aspects: (1) an understanding of the structure of flow with sudden

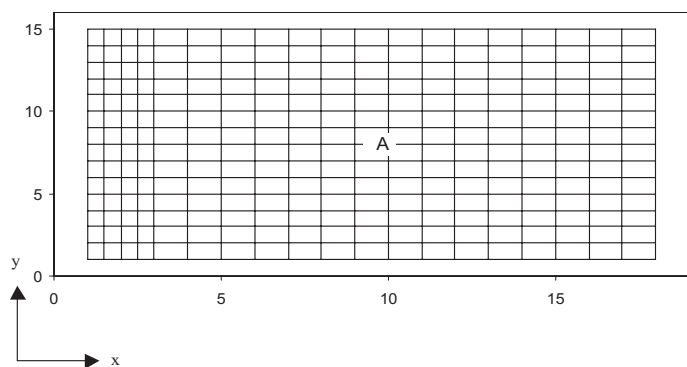


Fig. 6. Horizontal mesh used for the simulation of tide induced circulation

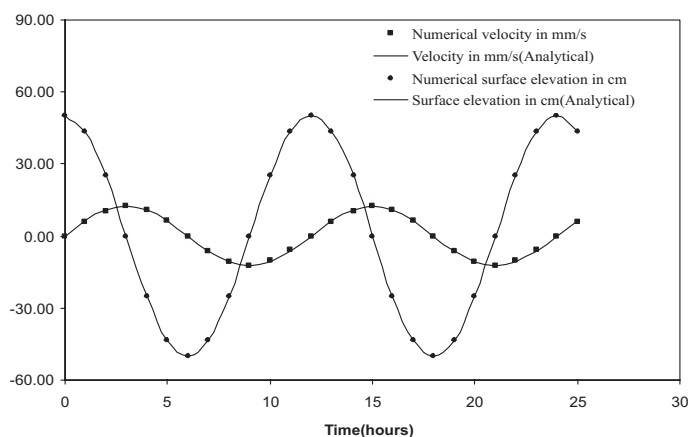


Fig. 7. Comparison of analytical and computed surface elevation and depth-averaged u -velocities, at A (Fig. 6)

contraction and expansion, and (2) verification of the three-dimensional hydrodynamic model developed in section 3.

The experiments were conducted in a rectangular flume with a depth of 0.6m, a length of 8m and a width of 1.2m. An opening with a depth of 0.5m, a length of 0.2m and a width of 0.2m was made in the flume. Fig. 8(a) shows the plan layout of the experimental apparatus. Fig. 8(b) shows the longitudinal view along the centerline of the flume. The coordinate system is also shown in Fig. 8(a) and (b). In the hydraulic experiment, only steady flow is studied. To minimize the influence of secondary flow on the main flow, water depth was set to be small compared to the width of the flume. Thus, the flow discharge in the flume was maintained constant at 20 liters per second and the water depth downstream of the opening was adjusted to about 28cm by controlling the tail gate. The Reynolds number upstream of the opening ($Re = \frac{UR}{\nu} = 5(\text{cm/s}) \times 20(\text{cm}) / 0.009(\text{cm}^2/\text{s}) \approx 11000$) was approximately 11000. It can be seen from the experiments that the state of flow upstream of the opening was quite stable, but the flow downstream of the opening was very unstable and strongly turbulent. The velocity in the flume was measured using an Electromagnetic Current Meter. The meter can be set in three measurement ranges ($0 \sim \pm 25$ cm/s, $0 \sim \pm 50$ cm/s and $0 \sim \pm 250$ cm/s).

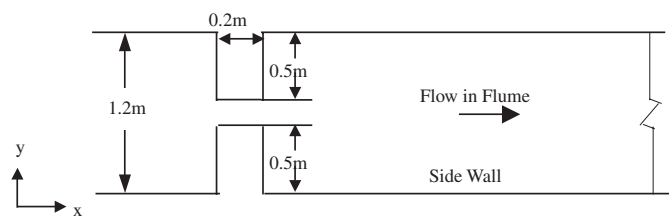


Fig. 8(a) Plan Layout

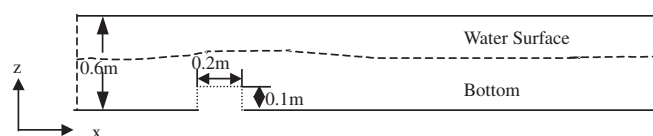


Fig. 8(b) Layout of Experimental Apparatus

Fig. 8. Layout of Experimental Apparatus

Its measurement accuracy is $\pm 2\%$ of the range or ± 0.5 mm/s. The two horizontal velocity components at the measured point can be obtained by two pairs of the electrodes installed in the sensor. The distributions of two velocity components along vertical lines and water depths at many locations were measured. In general, five point velocities were measured in one vertical line. The water depths in the flume were measured with a water surface sensor probe. Upstream of the opening, it is easy to measure the velocities and water depths. However, it is difficult to measure the velocities and water depths downstream of the opening since the flow is highly turbulent. In the present series of experiments, a series of velocity and water depth observations at a measurement point were made over a sufficient time interval and were averaged for removing the effect of temporal fluctuations of turbulent flow velocity.

5.2 Numerical simulation of hydraulic experiment

The validity of the hydrodynamic model is examined by comparing the numerical simulation results with the hydraulic experimental data. The flow domain for analysis includes 0.6m upstream of the area of the opening and 3.0m downstream of the opening. The flow domain was divided into twelve layers. To fit the complex bottom boundary, the layer thickness varied non-uniformly with water depth. The layer thickness was chosen as

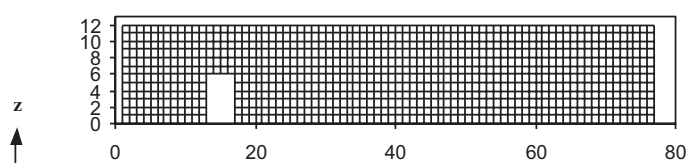


Fig. 9(a) Vertical Mesh

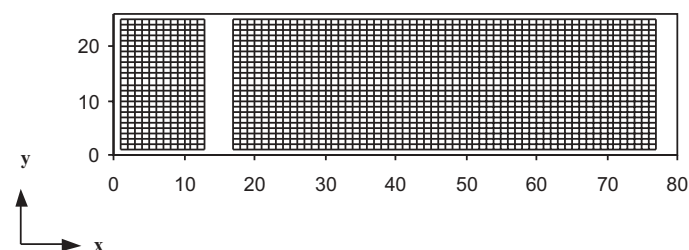


Fig. 9(b) Horizontal Mesh below the Sixth Layer

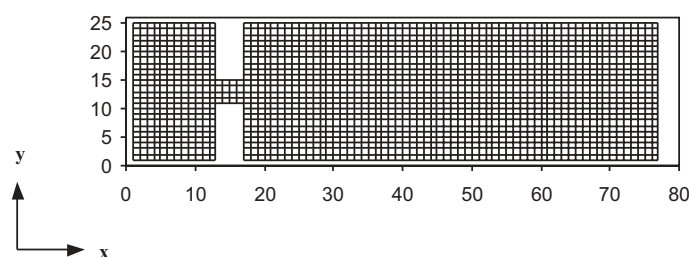
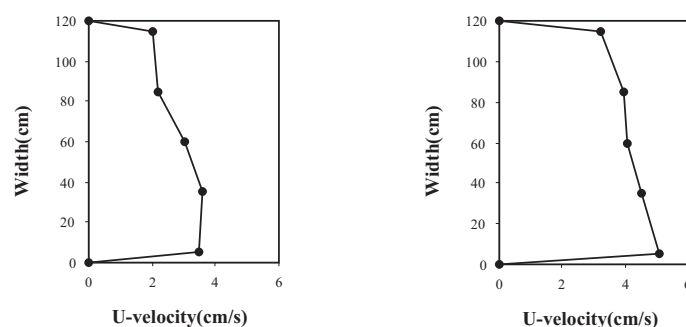


Fig. 9(c) Horizontal Mesh above the Seventh Layer

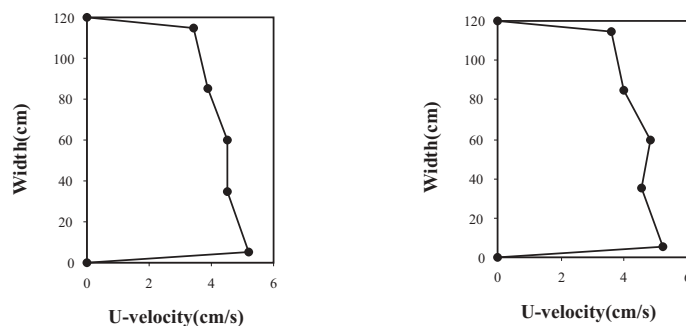
Fig. 9. Horizontal and Vertical Meshes Used for the Simulation of Sudden Contraction and Expansion Flow

1.5cm from the first layer to the fourth layer. The layer thickness was adopted as 2.0cm from the fifth layer to the seventh layer and 3.0cm from the eighth layer to the eleventh layer. The thickness of the twelfth layer was computed and changed with the location. The horizontal and vertical meshes are shown in Fig. 9. Figure 9(c) shows the horizontal mesh above the seventh layer. Figure 9(b) is the horizontal mesh below the sixth layer. Figure 9(a) shows the vertical mesh. The values of other parameters adopted are: $\Delta x = 0.05$ m; $\Delta y = 0.05$ m; $\Delta t = 0.005$ s; $\epsilon_h = 30$ cm²/s; $f = 0$; $\rho = 1000$ kg/m³; $\epsilon_z = 0.5$ cm²/s near the flume bottom below sixth layer, but $\epsilon_z = 1.2$ cm²/s away from the flume bottom above seventh layer. The values of ϵ_h and ϵ_z are estimated based on the gradients of velocity using the established relationships (Abbott, 1997; Kim and Lee, 1994). The velocity boundary condition was imposed at the upstream boundary. Five measurement vertical lines were uniformly arranged in the boundary cross-section and four measurement points were chosen in every measurement vertical line. Further, some measurement points were also arranged at the same layer. The velocities of the grid points in the other layers and cross-sectional direction on the upstream boundary were obtained by linear interpolations of the above measurement points. Figure 10 exhibits the measured velocity distribution of the four layers on the upstream boundary of the opening. It is observed that the velocities at the upstream boundary decrease gradually from one side of the channel to the other resulting in non-symmetrical incoming flow. The asymmetry in the flow is caused by imperfect boundary roughness and flow disturbances at the upstream inlet. The water elevation boundary condition was adopted at the downstream boundary 3.0m from the opening. Five



(a) First Layer

(b) Third Layer



(c) Seventh Layer

(d) Eleventh Layer

Fig. 10. Measured Velocity Change in Different Layers of Upstream Boundary

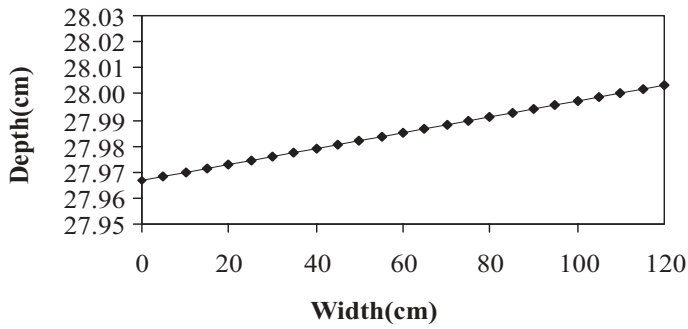


Fig. 11. Water Elevation at Downstream Boundary

measurement points of water surface elevation were uniformly laid in the downstream boundary cross-section. Figure 11 shows the measured water depth variation at the downstream boundary of the opening. The free surface elevations at the other grid points on the downstream boundary were obtained by linear interpola-

tions of the five measurement points. Non-slip boundary condition was used at the bottom boundary. Slip boundary conditions were imposed on the channel walls. The convergence was reached from a cold start after the program was run for ninety time-step lengths on a Pentium 200 MHz personal computer. The simulation run time was about 1.5 hours. Some preliminary numerical tests were carried out using different number of layers for the simulation of experimental study to test the grid dependency on the results. It was observed that there were no significant changes in the computed values of the velocities for the case tested.

Figure 12 presents comparisons of simulated flow velocities in the x direction with the experimental data along the centerline of the flume. The titles of the sub-figures indicate the horizontal locations of vertical velocity lines. The simulated flow velocities show reasonable agreements with the measured values both in front of the opening and behind the opening. The velocity compo-

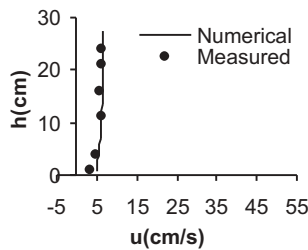


Fig. 12(a) Location(5,13)

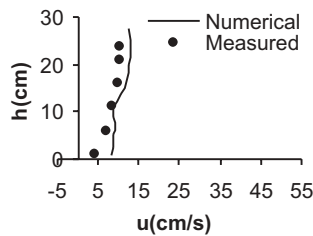


Fig. 12(b) Location(9,13)

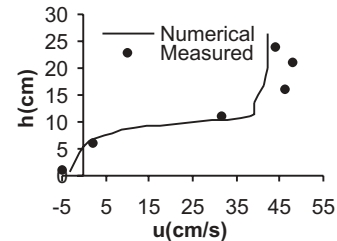


Fig. 12(c) Location(19,13)

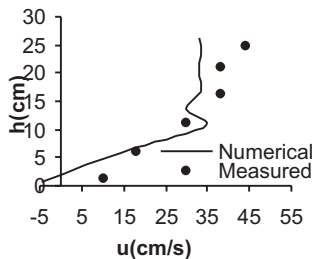


Fig. 12(d) Location(27,13)

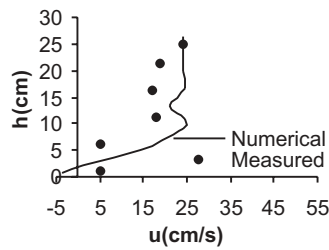


Fig. 12(e) Location(37,13)

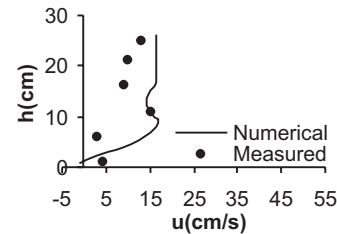


Fig. 12(f) Location(47,13)

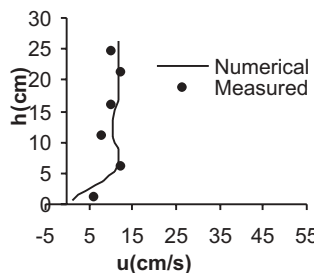


Fig. 12(g) Location(55,13)

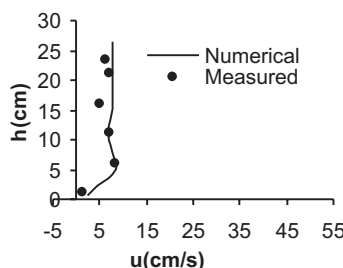


Fig. 12(h) Location(67,13)

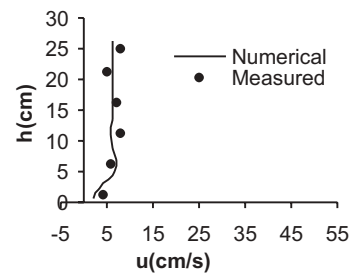


Fig. 12(i) Location(75,13)

Fig. 12. Comparisons of Simulated u-velocity Profiles with Experimental Data Along the Centerline of Flume (from Fig. 12(a) to Fig. 12(i))

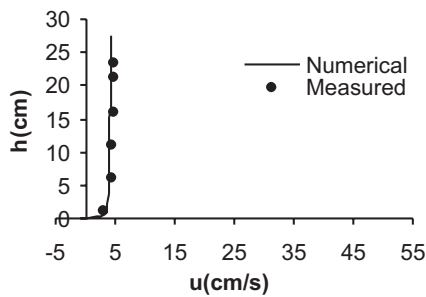


Fig. 13(a) Location(7,7)

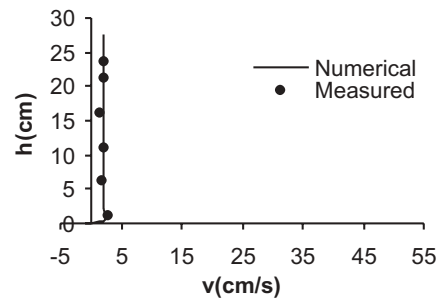


Fig. 13(b) Location(7,7)

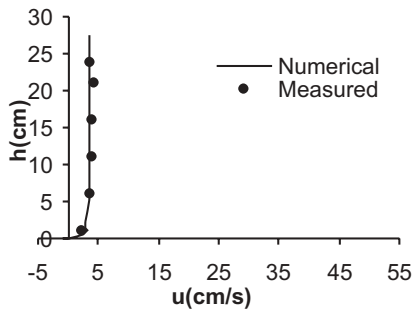


Fig. 13(c) Location(7,19)

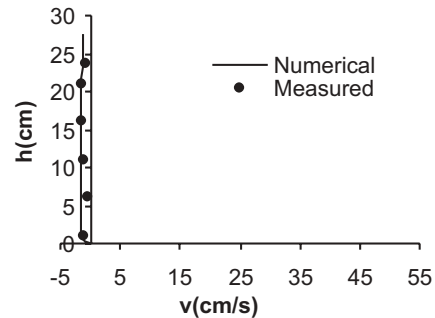


Fig. 13(d) Location(7,19)

Fig. 13. Comparisons of Computed u- and v-velocity Profiles with Experimental Data Upstream of the Opening

ment in the x direction changes greatly with the distance along the centerline of the flume and an eddy occurs apparently in the vertical direction downstream of the opening. Large differences exist between the simulated flow velocity and the measured value in the immediate vicinity of the opening due to strong turbulence. The major discrepancies between the calculated and measured values of velocity downstream of the opening are 6 cm/s in Fig. 12(c) and 10 cm/s in Fig. 12(d). These deviations are of the order of 13 percent and 22 percent of the measured values. They occur at about 21 cm of water depth and free water surface. Figures 13 to 14 show the simulated and measured flow velocity profiles in x and y directions of four vertical lines upstream and downstream of the opening. Major discrepancy between calculated and measured values is noted at locations (31,7) and (31,19) in Fig. 14. These locations are situated in the downstream eddy region where the flow is highly turbulent. The component values of velocities at these points are small and the flow direction changes quickly. Discrepancies in the eddy region are expected as numerical simulation of flow structure in the eddy would need the use of a refined turbulent model such as $k-\epsilon$ turbulent model. Generally there is reasonable agreement between the simulated flow velocity components and the measured values. Further, it is observed that the simulated velocities upstream of the opening are in better agreement with the experimental data than downstream of the opening.

The flow structure is presented in Figs. 15, 16, 17 and 18. Figure 15(b) shows the simulated flow pattern in the x and z plane along the centerline of the channel. It is apparent that the flow velocities increase rapidly when the flow is close to the opening, but the flow velocities decrease with eddy formation in the vertical direction downstream of the opening. Further Figure 15(a) focuses on the flow pattern in the vicinity of the opening. Figure 16 illus-

trates the simulated flow patterns in the x - y plane at four layers (first layer, fourth layer, seventh layer and eleventh layer). It is shown that the flow velocities change gradually and the flow state is stable in front of the opening. However, the flow velocities change rapidly and the flow state is very unstable behind the opening due to the formation of eddies. Two large-scale and non-symmetrical horizontal eddies are formed downstream of the opening because of slightly non-symmetrical incoming flow from the upstream of the opening as a result of the nonsymmetrical measured velocity distribution imposed as an upstream boundary condition. Moreover, Figure 16(a) to Figure 16(d) show clearly that there exists the great depth-wise change of flow states. At lower layers water flow is complicated and the circulation in the cross-sectional direction is obvious and strong. Figures 17 and 18 show the simulated flow patterns in the y - z plane at the distances of 35cm (Fig. 17(b)) and 5cm (Fig. 17(a)) upstream of the opening and 5cm (Fig. 18(a)), 155cm (Fig. 18(b)) and 275cm (Fig. 18(c)) downstream of the opening. It is apparent that the flow will converge when it approaches the opening. The flow stream will dive down and form back-flow around the main jet stream. The complex circulation in the cross-section is formed as the flow is away from the opening. Comparison between Fig. 17 and Fig. 18 also indicates that the flow structures are much more complex downstream of the opening than upstream of the opening in a sudden contraction and expansion flow.

In the numerical simulation of the hydraulic experiment, the variable ϵ_z values in the different layers were tested. Curve 1 in Fig. 19 shows the numerical results at the horizontal location (19,13) when $\epsilon_z = 0.5 \text{ cm}^2/\text{s}$ near the flume bottom below sixth layer, but $\epsilon_z = 1.2 \text{ cm}^2/\text{s}$ away from the flume bottom above seventh layer. Curve 2 in Fig. 19 shows the numerical results when $\epsilon_z = 1.2 \text{ cm}^2/\text{s}$ in the whole domain. It was found that the simulation re-

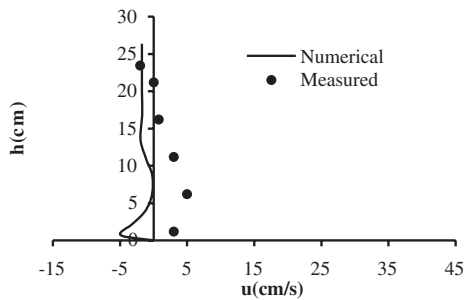


Fig. 14(a) Location(31,7)

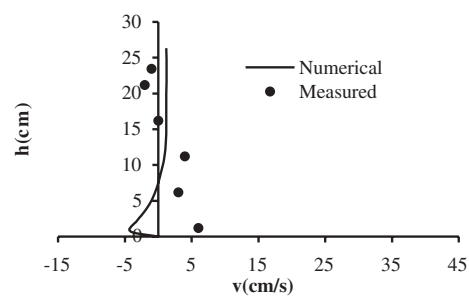


Fig. 14(b) Location(31,7)

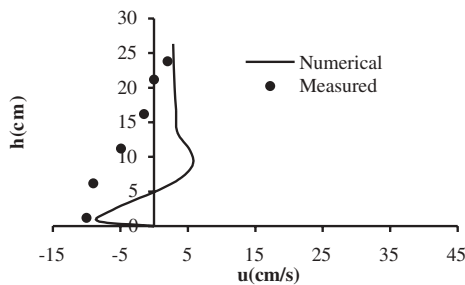


Fig. 14(c) Location(31,19)

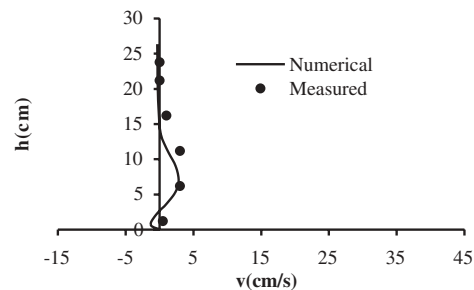


Fig. 14(d) Location(31,19)

Fig. 14. Comparisons of Computed u - and v -velocity Profiles with Experimental Data Downstream of the Opening

sults were slightly improved when the vertical eddy viscosity coefficient ϵ_z was reduced near the flume bottom.

By using the three-dimensional multi-level hydrodynamic model, the depth-wise variations in flow velocity are easily seen. The simulated flow velocities reasonably represent the actual flow conditions in the channel with a sudden contraction and expansion structure.

6 Conclusions

Flow characteristics in an open channel with a constriction were investigated experimentally and numerically. Based on the results of the study, the following conclusions are drawn:

1. The comparisons of numerical simulation results with the experimental data show that the developed three-dimensional multi-level hydrodynamic model is efficient and applicable to simulate complex flows such as a sudden contraction and expansion flow to a reasonable degree of accuracy.
2. The numerical and experimental results illustrate that the flow in an open channel with an opening is very complicated. The flow in front of the opening is stable and less turbulent whilst the flow beyond the opening is very unstable with strong turbulence. Downstream of the opening, eddies are formed in the vertical and cross-sectional planes as well as in the horizontal

plane.

3. In the three-dimensional numerical model, the two-step Euler predictor-corrector algorithm was introduced to predict and correct the free surface water level more accurately. The momentum equations are solved using explicit schemes, and the continuity equation is solved using an implicit scheme. The numerical model developed in this study is found to be efficient and simple.
4. The numerical simulation results are sensitive to vertical diffusion coefficient compared to other parameters. Variable ϵ_z values in the different layers were tested. The simulation results were improved when the vertical diffusion coefficient ϵ_z was reduced near the flume bottom. In order to give better simulation for sudden contraction and expansion water flows, it is necessary to assess the values of ϵ_z more accurately by using turbulent energy model in future research work.

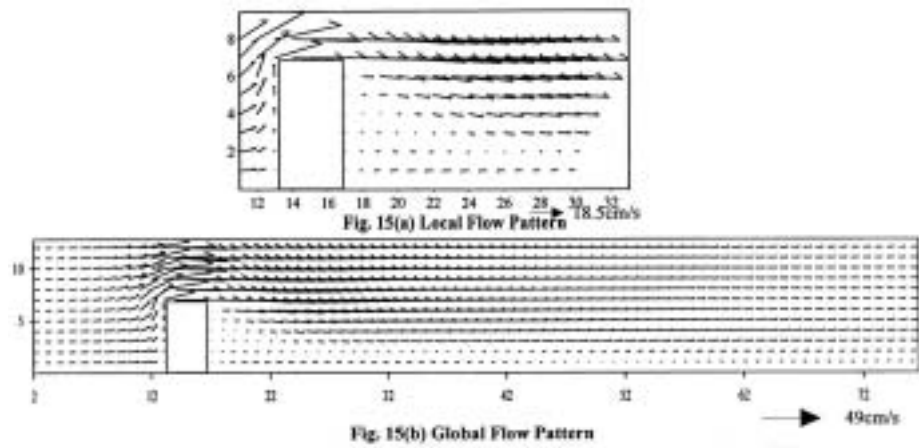


Fig. 15. Simulated Vertical Flow Patterns along the Centerline of Flume

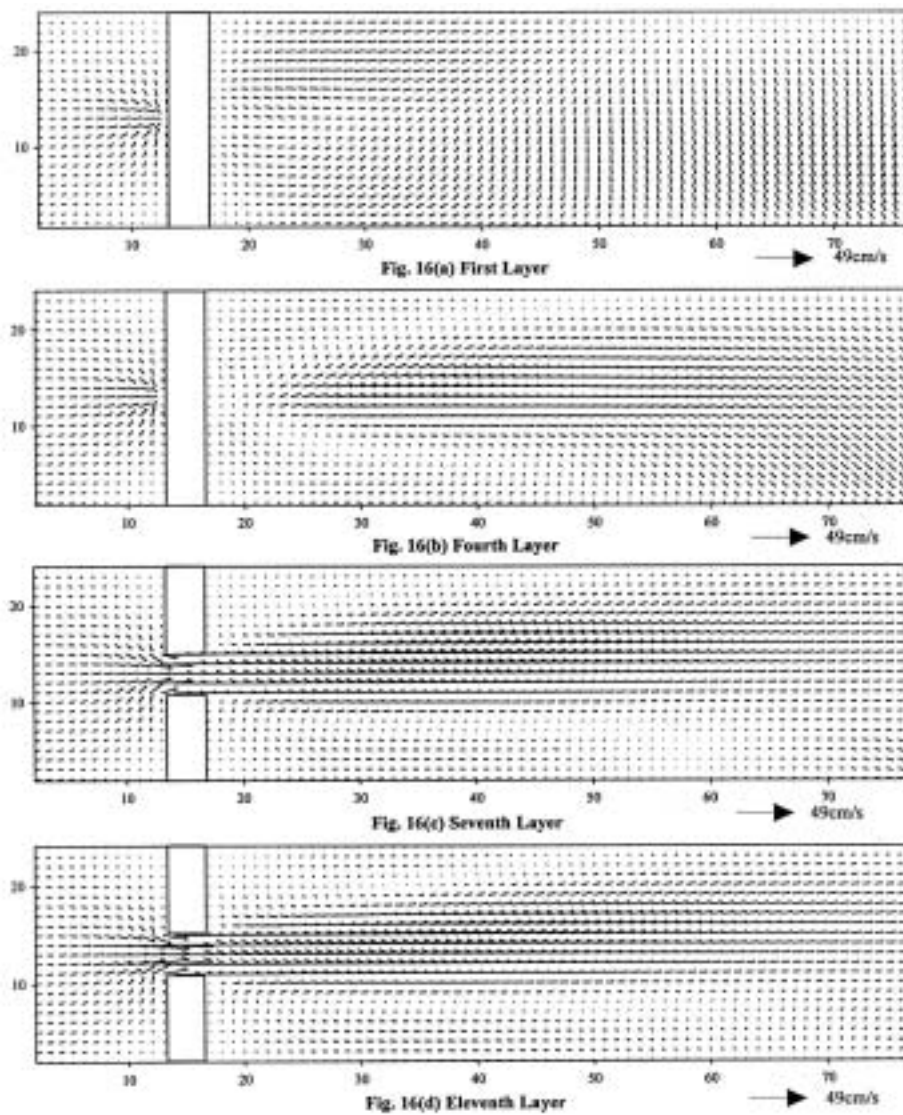


Fig. 16. Simulated Horizontal Flow Patterns at Various Layers

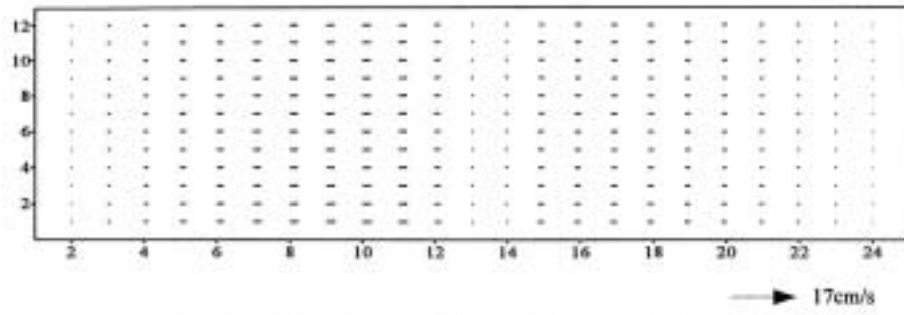


Fig. 17(a) at the Distance of 35cm(i=6) Upstream of the Opening

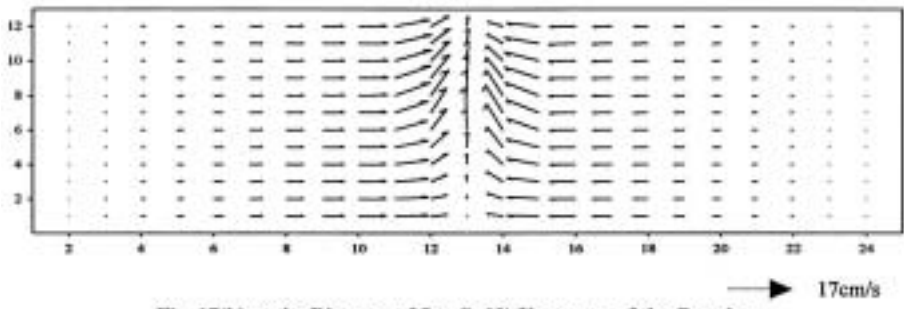


Fig. 17(b) at the Distance of 5cm(i=12) Upstream of the Opening

Fig. 17. Simulated Flow Patterns in y-z Plane Upstream of the Opening

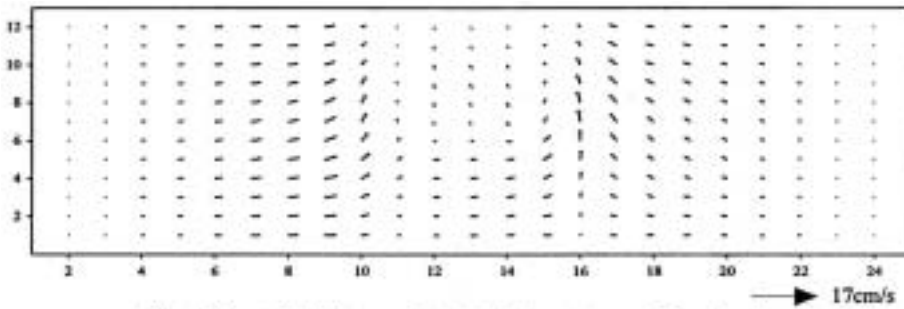


Fig. 18(a) at the Distance of 5cm(i=18) Downstream of the Opening

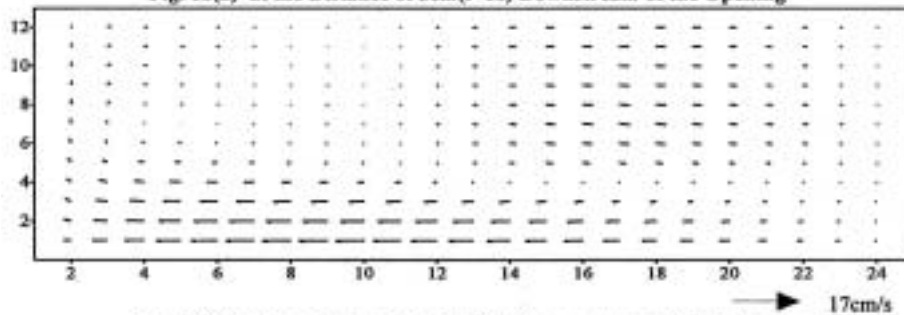


Fig. 18(b) at the Distance of 155cm(i=48) Downstream of the Opening

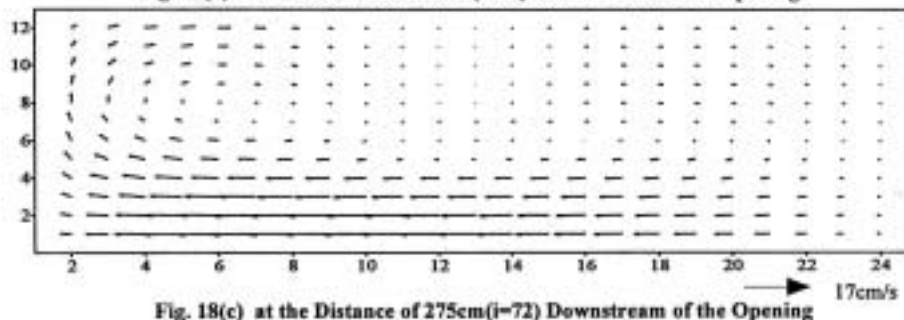


Fig. 18(c) at the Distance of 275cm(i=72) Downstream of the Opening

Fig. 18. Simulated Flow Patterns in y-z Plane Downstream of the Opening

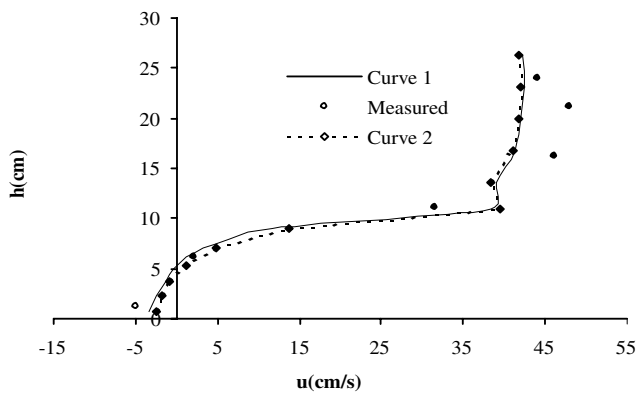


Fig. 19. Comparison of Computed U-velocity Profiles with Different Vertical Eddy Viscosity at Location(19,13)

Appendix I: References

- ABBOTT, M. B. 1997. "Range of Tidal Flow Modeling", *Journal of Hydraulic Engineering*, ASCE, Vol. 123, No. 4, pp.257-275.
- ADAMS, E. W. and RODI, W. 1990. "Modeling Flow and Mixing in Sedimentation Tanks", *Journal of Hydraulic Engineering*, ASCE, Vol. 116, No. 7, pp. 895-913.
- CAO, Z. D. and ZHANG, Y. P. 1987. "A Three-dimensional Numerical Model for Tide Flow and Transport of spilled oil"(in Chinese), Internal Report, Tianjin Institute of Water-transportation Engineering, Tianjin, P. R. China.
- CHENG, R. T. and SMITH, P. E. 1989. "A Survey of Three-dimensional Numerical Models", *Estuarine and Coastal Modeling*, in *Estuarine and Coastal Modeling*, Spaulding. M. L.(Ed.), ASCE. pp. 1-15.
- DANIEL, R. L. and FRANCISCO, E. W. 1987. "Three-dimensional Hydrodynamics on Finite Elements. Part I: Linearized Harmonic Model", *International Journal for Numerical Methods in Fluids*, Vol. 7, pp. 871-909.
- FANG, H. W. 1994. "Three-dimensional Alternating-direction Finite Analytic Method"(in Chinese), *Journal of Hydrodynamics*, Ser. A, Vol. 9, No.5, pp. 557-565.
- IPPEN, A. T. 1966. *Estuary and Coastline Hydrodynamics*, McGraw Hill, New York.
- KARPIK, S. R. and RAITHEY, G. D. 1990. "Laterally Averaged Hydrodynamics Model for Reservoir Predictions", *Journal of Hydraulic Engineering*, ASCE, Vol. 116, No. 6, pp. 783-798.
- KAWAHARA, M., KOBAYASHI, M. and NAKATA, K. 1983. "Multiple Level Finite Element Analysis and Its Applications to Tidal Current Flow in Tokyo Bay", *Appl. Math. Modeling*, Vol. 7, pp. 197-211.
- KIM, C. and LEE, 1994. "A Three-dimensional PC-based Hydrodynamic Model Using An ADI Scheme", *Coastal Engineering* 23, pp. 271-287.
- LEENDERTSE, J. J., ALEXANDER, R. C. and LIU, S. K. 1973. "Three-dimensional Model for Estuaries and Coastal Seas", *Rand Corp.*, Vol. I, R-1417-OWRR.
- LI, Y. S. and ZHAN, J. M. 1993. "An Efficient Three-dimensional Semi-implicit Finite Element Scheme for Simulation of Free Surface Flows", *International Journal for Numerical Methods in Fluids*, Vol. 16, pp. 187-198.
- LU, Q. M. and WAI, W. H. 1995. "Three-dimensional Tidal Flow Numerical Model for Coastal and Estuarine Shallow Waters"(in Chinese), *The Ocean Engineering*, Vol. 13, No.4, pp. 47-60.
- MUTSUTO, K. and KENICHI, H. 1978. "Periodic Galerkin Finite Element Method of Tidal Flow", *International Journal for Numerical Methods in Engineering*, Vol. 12, pp. 115-127.
- SHANKAR, N. J., CHEONG, H. F. and SANKARANARAYANAN, S. 1995. "Multilevel Finite Difference Model for Three-dimensional Hydrodynamic Circulation", Internal Report, Dept. of Civil Engineering, National University of Singapore, Singapore.
- SHINJI, S. 1996. "Effects of Winds and Breaking Waves on Large-scale Coastal Currents Developed by Winter Storms in Japan", *Coastal Engineering in Japan*, Vol. 39, No. 2, pp. 129-143
- TAWATCHAI, T. and SELVARATNAM, M. 1990. "2-D Depth-Averaged Flow Computation near Groyne", *Journal of Hydraulic Engineering*, ASCE, Vol. 116, No. 1, pp. 71-86.
- TOMOYA, S. and PUN, K. L. 1992. "Multi-level Model for Hydrodynamic Circulation and Dispersion Process in Bays", *Coastal Engineering in Japan*, Vol. 35, No. 1, pp. 49-66.
- ZHOU, S. and JOHN, A. M. 1992. "Modeling of Rectangular Settling Tanks", *Journal of Hydraulic Engineering*, ASCE, Vol. 118, No. 10, pp. 1391-1405.
- ZHANG, Q. Y. 1998. "3-D Circulation in Steady and Unsteady Free Surface Flows", M. Eng. Thesis, National University of Singapore, Singapore.

Appendix II: Notations

A	tide amplitude
c_s	wind stress coefficient
f	Coriolis force coefficient
g	magnitude of gravitational acceleration
h	water depth
H	water depth below reference plane
p	temporal mean pressure
t	time
u	temporal mean velocity in x direction
U	depth-averaged velocity in x direction
v	temporal mean velocity in y direction
V	depth-averaged velocity in y direction
w	temporal mean velocity in z direction
W	wind speed
x	longitudinal coordinate in Cartesian system.
y	lateral coordinate in Cartesian system
z	vertical coordinate in Cartesian system

Greek Symbols

Δt	time step length
$\Delta x, \Delta y$	space step lengths in x, y directions

ε	turbulent energy dissipation rate
ε_x	eddy viscosity coefficient in x direction
ε_y	eddy viscosity coefficient in y direction
ε_z	eddy viscosity coefficient in z direction
ε_h	eddy viscosity coefficient in the horizontal direction
k	turbulent energy
ρ	fluid density
σ	$(h+z)/(h+\zeta)$
τ	shear stress
ω	rotational angular velocity of Earth
ζ	surface elevation above reference plane

Subscripts

a	air
b	bottom
h	horizontal direction
k	layer number
s	surface
i, j, k	location of grid point

Superscripts

n	number of time step lengths
s	surface

Appendix III

The finite difference equations for predicting free surface elevation are:

$$\frac{\zeta_{i,j}^{n+1} - \zeta_{i,j}^{n-1}}{2\Delta t} = w_{i,j,L+\frac{1}{2}}^n \quad t \geq 2\Delta t \quad (\text{III-1})$$

$$\frac{\zeta_{i,j}^{n+1} - \zeta_{i,j}^n}{\Delta t} = w_{i,j,L+\frac{1}{2}}^n \quad t = \Delta t \quad (\text{III-2})$$

The finite difference equation for correcting water surface elevation is:

$$\frac{\zeta_{i,j}^{n+1} - \zeta_{i,j}^n}{\Delta t} = (w_{i,j,L+\frac{1}{2}}^{n+1} + w_{i,j,L+\frac{1}{2}}^n) / 2 \quad (\text{III-3})$$

After two coordinate functions $(x(i))$ and $(y(j))$ of grid nodes are introduced for non-uniform grids, the definition can be made that for a grid node (i, j, k) , its x coordinate is $x(i)\Delta x$, its y coordinate is $y(j)\Delta y$ and it is located at the center of k -th layer. Δx and Δy are space step lengths in the x and y directions for a uniform grid. Δx and Δy are maximum distances between two nodes in x and y directions for non-uniform grid. The finite difference equation for vertical velocity w can be obtained by discretizing equation(5) in a uniform grid or non-uniform grid.

$$w_{i,j,k+\frac{1}{2}}^{n+1} = w_{i,j,k-\frac{1}{2}}^{n+1} - h_{k,i,j,k}^{n+1} \left\langle \frac{\partial u}{\partial x} \right\rangle_{i,j,k}^{n+1} - u_{i,j,k}^{n+1} \left\langle \frac{\partial h_k}{\partial x} \right\rangle_{i,j,k}^{n+1} - h_{k,i,j,k}^{n+1} \left\langle \frac{\partial v}{\partial y} \right\rangle_{i,j,k}^{n+1} - v_{i,j,k}^{n+1} \left\langle \frac{\partial h_k}{\partial y} \right\rangle_{i,j,k}^{n+1} \quad (\text{III-4})$$

where

$$u_{i,j,k}^{n+1} \approx \frac{1}{2}(u_{i+1,j,k}^{n+1} + u_{i-1,j,k}^{n+1})$$

$$v_{i,j,k}^{n+1} \approx \frac{1}{2}(v_{i,j+1,k}^{n+1} + v_{i,j-1,k}^{n+1})$$

$$\left\langle \frac{\partial u}{\partial x} \right\rangle_{i,j,k}^{n+1} = (u_{i+1,j,k}^{n+1} - u_{i-1,j,k}^{n+1}) / ((x(i+1) - x(i-1))\Delta x)$$

$$\left\langle \frac{\partial v}{\partial y} \right\rangle_{i,j,k}^{n+1} = (v_{i,j+1,k}^{n+1} - v_{i,j-1,k}^{n+1}) / ((y(j+1) - y(j-1))\Delta y)$$

$$\left\langle \frac{\partial h_k}{\partial x} \right\rangle_{i,j,k}^{n+1} = (h_{k,i+2,j,k}^{n+1} - h_{k,i,j,k}^{n+1}) / (2(x(i+2) - x(i))\Delta x) + (h_{k,i,j,k}^{n+1} - h_{k,i-2,j,k}^{n+1}) / (2(x(i) - x(i-2))\Delta x)$$

$$\left\langle \frac{\partial h_k}{\partial y} \right\rangle_{i,j,k}^{n+1} = (h_{k,i,j+2,k}^{n+1} - h_{k,i,j,k}^{n+1}) / (2(y(j+2) - y(j))\Delta y) + (h_{k,i,j,k}^{n+1} - h_{k,i,j-2,k}^{n+1}) / (2(y(j) - y(j-2))\Delta y)$$

The finite difference equation for horizontal velocity component u can be obtained by expanding and discretizing the equation (6) in uniform grid or non-uniform grid.

$$u_{i,j,k}^{n+1} = \{u_{i,j,k}^n - \frac{\Delta t}{h_{k,i,j,k}^{n+1}}(u_{i,j,k}^n v_{i,j,k}^n \left\langle \frac{\partial h_k}{\partial y} \right\rangle_{i,j,k}^{n+1} + \bar{v}_{i,j,k}^n \bar{h}_{k,i,j,k}^{n+1} \left\langle \frac{\partial u}{\partial y} \right\rangle_{i,j,k}^n + \langle \bar{w}u \rangle_{i,j,k-\frac{1}{2}}^n - \langle \bar{w}u \rangle_{i,j,k+\frac{1}{2}}^n + u_{i,j,k}^n u_{i,j,k}^n \left\langle \frac{\partial h_k}{\partial x} \right\rangle_{i,j,k}^{n+1}) + \Delta t f \bar{v}_{i,j,k}^n - \Delta t g \left\langle \frac{\partial \zeta}{\partial x} \right\rangle_{i,j,k}^{n+1} + \varepsilon_h \Delta t \left\langle \frac{\partial^2 u}{\partial x^2} \right\rangle_{i,j,k}^n + \varepsilon_h \Delta t \left\langle \frac{\partial^2 u}{\partial y^2} \right\rangle_{i,j,k}^n + \frac{\varepsilon_z \Delta t}{h_{k,i,j,k}^{n+1}} \left\langle \frac{\partial u}{\partial z} \right\rangle_{i,j,k+\frac{1}{2}}^n - \frac{\varepsilon_z \Delta t}{h_{k,i,j,k}^{n+1}} \left\langle \frac{\partial u}{\partial z} \right\rangle_{i,j,k-\frac{1}{2}}^n\} / \{1 + 2\Delta t \left\langle \frac{\partial u}{\partial x} \right\rangle_{i,j,k}^n + \Delta t \left\langle \frac{\partial v}{\partial y} \right\rangle_{i,j,k}^n\} \quad (\text{III-5})$$

Where

$$\bar{h}_{k,i,j,k}^{n+1} \approx \frac{1}{2}(h_{k,i+1,j,k}^{n+1} + h_{k,i-1,j,k}^{n+1})$$

$$\bar{v}_{i,j,k}^n \approx \frac{1}{4}(v_{i+1,j+1,k}^n + v_{i+1,j-1,k}^n + v_{i-1,j+1,k}^n + v_{i-1,j-1,k}^n)$$

$$\langle \bar{w}u \rangle_{i,j,k-\frac{1}{2}}^n \approx \frac{1}{4}(w_{i+1,j,k-1}^n + w_{i-1,j,k-1}^n)(u_{i,j,k-1}^n + u_{i,j,k}^n)$$

$$\langle \bar{w}u \rangle_{i,j,k+\frac{1}{2}}^n \approx \frac{1}{4}(w_{i+1,j,k}^n + w_{i-1,j,k}^n)(u_{i,j,k+1}^n + u_{i,j,k}^n)$$

$$\left\langle \frac{\partial \zeta}{\partial x} \right\rangle_{i,j,k}^{n+1} = (\zeta_{i+1,j,k}^{n+1} - \zeta_{i-1,j,k}^{n+1}) / ((x(i+1) - x(i-1))\Delta x)$$

$$\left\langle \frac{\partial h_k}{\partial x} \right\rangle_{i,j,k}^{n+1} = (h_{ki+1,j,k}^{n+1} - h_{ki-1,j,k}^{n+1}) / ((x(i+1) - x(i-1))\Delta x)$$

$$\left\langle \frac{\partial h_k}{\partial y} \right\rangle_{i,j,k}^{n+1} = (h_{ki+1,j+2,k}^{n+1} - h_{ki+1,j,k}^{n+1} + h_{ki-1,j+2,k}^{n+1} - h_{ki-1,j,k}^{n+1}) / ((y(j+2) - y(j))4\Delta y) + (h_{ki+1,j,k}^{n+1} - h_{ki+1,j-2,k}^{n+1} + h_{ki-1,j,k}^{n+1} - h_{ki-1,j-2,k}^{n+1}) / ((y(j) - y(j-2))4\Delta y)$$

$$\left\langle \frac{\partial u}{\partial y} \right\rangle_{i,j,k}^n = (u_{i,j+2,k}^n - u_{i,j,k}^n) / ((y(j+2) - y(j))2\Delta y) + (u_{i,j,k}^n - u_{i,j-2,k}^n) / ((y(j) - y(j-2))2\Delta y)$$

$$\left\langle \frac{\partial u}{\partial z} \right\rangle_{i,j,k+\frac{1}{2}}^n = \frac{1}{4} (u_{i,j,k+1}^n - u_{i,j,k}^n) / \bar{h}_{ki,j,k}^{n+1}$$

$$\left\langle \frac{\partial u}{\partial z} \right\rangle_{i,j,k-\frac{1}{2}}^n = \frac{1}{4} (u_{i,j,k}^n - u_{i,j,k-1}^n) / \bar{h}_{ki,j,k}^{n+1}$$

$$\left\langle \frac{\partial v}{\partial y} \right\rangle_{i,j,k}^n = (v_{i+1,j+1,k}^n + v_{i-1,j+1,k}^n - v_{i+1,j-1,k}^n - v_{i-1,j-1,k}^n) / ((y(j+1) - y(j-1))2\Delta y)$$

$$\left\langle \frac{\partial v}{\partial y} \right\rangle_{i,j,k}^n = (v_{i+1,j+1,k}^n + v_{i-1,j+1,k}^n - v_{i+1,j-1,k}^n - v_{i-1,j-1,k}^n) / ((y(j+1) - y(j-1))2\Delta y)$$

$$\left\langle \frac{\partial^2 u}{\partial x^2} \right\rangle_{i,j,k}^n = ((u_{i+2,j,k}^n - u_{i,j,k}^n) / ((x(i+2) - x(i))\Delta x) - (u_{i,j,k}^n - u_{i-2,j,k}^n) / ((x(i) - x(i-2))\Delta x)) / \left(\frac{1}{2} (x(i+2) - x(i-2))\Delta x \right)$$

for $u_{i,j,k}^n \leq 0$

$$\left\langle \frac{\partial u}{\partial x} \right\rangle_{i,j,k}^n = (u_{i+2,j,k}^n - u_{i,j,k}^n) / ((x(i+2) - x(i))\Delta x)$$

for $u_{i,j,k}^n > 0$

$$\left\langle \frac{\partial u}{\partial x} \right\rangle_{i,j,k}^n = (u_{i,j,k}^n - u_{i-2,j,k}^n) / ((x(i) - x(i-2))\Delta x)$$

On the analogy of the equation (6), the finite difference equation for the horizontal velocity component v can be obtained by discretizing equation (7):

$$\begin{aligned} v_{i,j,k}^{n+1} &= \{v_{i,j,k}^n - \frac{\Delta t}{\bar{h}_{ki,j,k}^{n+1}} (\bar{u}_{i,j,k}^{n+1} v_{i,j,k}^n \left\langle \frac{\partial h_k}{\partial x} \right\rangle_{i,j,k}^{n+1} + \bar{u}_{i,j,k}^{n+1} \bar{h}_{ki,j,k}^{n+1} \left\langle \frac{\partial v}{\partial x} \right\rangle_{i,j,k}^n + \langle \bar{wv} \rangle_{i,j,k-\frac{1}{2}}^n - \langle \bar{wv} \rangle_{i,j,k+\frac{1}{2}}^n + v_{i,j,k}^n v_{i,j,k}^n \\ &\left\langle \frac{\partial h_k}{\partial y} \right\rangle_{i,j,k}^{n+1}) - \Delta t f \bar{u}_{i,j,k}^{n+1} - \Delta t g \left\langle \frac{\partial \zeta}{\partial y} \right\rangle_{i,j,k}^{n+1} + \varepsilon_h \Delta t \left\langle \frac{\partial^2 v}{\partial x^2} \right\rangle_{i,j,k}^n + \varepsilon_h \Delta t \left\langle \frac{\partial^2 v}{\partial y^2} \right\rangle_{i,j,k}^n + \frac{\varepsilon_z \Delta t}{\bar{h}_{ki,j,k}^{n+1}} \left\langle \frac{\partial v}{\partial z} \right\rangle_{i,j,k+\frac{1}{2}}^n - \frac{\varepsilon_z \Delta t}{\bar{h}_{ki,j,k}^{n+1}} \left\langle \frac{\partial v}{\partial z} \right\rangle_{i,j,k-\frac{1}{2}}^n \} / \\ &\{1 + \Delta t \left\langle \frac{\partial u}{\partial x} \right\rangle_{i,j,k}^{n+1} + 2\Delta t \left\langle \frac{\partial v}{\partial y} \right\rangle_{i,j,k}^n \} \end{aligned} \quad \text{(III-6)}$$

where

$$\bar{h}_{ki,j,k}^{n+1} \approx \frac{1}{2} (h_{ki,j+1,k}^{n+1} + h_{ki,j-1,k}^{n+1})$$

$$\bar{u}_{i,j,k}^n \approx \frac{1}{4} (u_{i+1,j+1,k}^n + u_{i+1,j-1,k}^n + u_{i-1,j+1,k}^n + u_{i-1,j-1,k}^n)$$

$$\langle \bar{wv} \rangle_{i,j,k-\frac{1}{2}}^n \approx \frac{1}{4} (w_{i,j-1,k-1}^n + w_{i,j+1,k-1}^n) (v_{i,j,k-1}^n + v_{i,j,k}^n)$$

$$\langle \bar{wv} \rangle_{i,j,k+\frac{1}{2}}^n \approx \frac{1}{4} (w_{i,j+1,k}^n + w_{i,j-1,k}^n) (v_{i,j,k+1}^n + v_{i,j,k}^n)$$

$$\left\langle \frac{\partial \zeta}{\partial y} \right\rangle_{i,j,k}^{n+1} = (\zeta_{i,j+1,k}^{n+1} - \zeta_{i,j-1,k}^{n+1}) / ((y(j+1) - y(j-1))\Delta y)$$

$$\left\langle \frac{\partial h_k}{\partial y} \right\rangle_{i,j,k}^{n+1} = (h_{ki,j+1,k}^{n+1} - h_{ki,j-1,k}^{n+1}) / ((y(j+1) - y(j-1))\Delta y)$$

$$\left\langle \frac{\partial h_k}{\partial x} \right\rangle_{i,j,k}^{n+1} = (h_{ki+2,j+1,k}^{n+1} - h_{ki,j+1,k}^{n+1} + h_{ki+2,j-1,k}^{n+1} - h_{ki,j-1,k}^{n+1}) / ((x(i+2) - x(i))4\Delta x) + (h_{ki-2,j+1,k}^{n+1} - h_{ki,j+1,k}^{n+1} + h_{ki-2,j-1,k}^{n+1} - h_{ki,j-1,k}^{n+1}) / ((x(i) - x(i-2))4\Delta x)$$

$$\left\langle \frac{\partial v}{\partial x} \right\rangle_{i,j,k}^n = (v_{i+2,j,k}^n - v_{i,j,k}^n) / ((x(i+2) - x(i))2\Delta x) + (v_{i,j,k}^n - v_{i-2,j,k}^n) / ((x(i) - x(i-2))2\Delta x)$$

$$\left\langle \frac{\partial v}{\partial z} \right\rangle_{i,j,k+\frac{1}{2}}^n = \frac{1}{4} (v_{i,j,k+1}^n - v_{i,j,k}^n) / \bar{h}_{ki,j,k}^{n+1}$$

$$\left\langle \frac{\partial v}{\partial z} \right\rangle_{i,j,k-\frac{1}{2}}^n = \frac{1}{4} (v_{i,j,k}^n - v_{i,j,k-1}^n) / \bar{h}_{ki,j,k}^{n+1}$$

$$\left\langle \frac{\partial u}{\partial x} \right\rangle_{i,j,k}^{n+1} = (u_{i+1,j+1,k}^{n+1} + u_{i+1,j-1,k}^{n+1} - u_{i-1,j+1,k}^{n+1} - u_{i-1,j-1,k}^{n+1}) / ((x(i+1) - x(i-1))2\Delta x)$$

$$\left\langle \frac{\partial^2 v}{\partial y^2} \right\rangle_{i,j,k}^n = ((v_{i,j+2,k}^n - v_{i,j,k}^n) / ((y(j+2) - y(j))\Delta y) - (v_{i,j,k}^n - v_{i,j-2,k}^n) / ((y(j) - y(j-2))\Delta y)) / \left(\frac{1}{2} (y(j+2) - y(j-2))\Delta y \right)$$

$$\left\langle \frac{\partial^2 v}{\partial x^2} \right\rangle_{i,j,k}^n = ((v_{i+2,j,k}^n - v_{i,j,k}^n) / ((x(i+2) - x(i))\Delta x) - (v_{i,j,k}^n - v_{i-2,j,k}^n) / ((x(i) - x(i-2))\Delta x)) / \left(\frac{1}{2} (x(i+2) - x(i-2))\Delta x \right)$$

for $v_{i,j,k}^n \leq 0$

$$\left\langle \frac{\partial v}{\partial y} \right\rangle_{i,j,k}^n = (v_{i,j+2,k}^n - v_{i,j,k}^n) / ((y(j+2) - y(j))\Delta y)$$

for $v_{i,j,k}^n > 0$

$$\left\langle \frac{\partial v}{\partial y} \right\rangle_{i,j,k}^n = (v_{i,j,k}^n - v_{i,j-2,k}^n) / ((y(j) - y(j-2))\Delta y)$$